



HAL
open science

Geophysical signature of the Tunnunik impact structure, Northwest Territories, Canada

Yoann Quesnel, W. Zylberman, P. Rochette, Minoru Uehara, Jérôme Gattacceca, G R Osinski, P. Dussouillez, C. Lepaulard, C. Champollion

► To cite this version:

Yoann Quesnel, W. Zylberman, P. Rochette, Minoru Uehara, Jérôme Gattacceca, et al.. Geophysical signature of the Tunnunik impact structure, Northwest Territories, Canada. *Meteoritics and Planetary Science*, 2020, 55 (3), pp.480-495. 10.1111/maps.13447 . insu-02484453v2

HAL Id: insu-02484453

<https://insu.hal.science/insu-02484453v2>

Submitted on 15 Dec 2023

HAL is a multi-disciplinary open access archive for the deposit and dissemination of scientific research documents, whether they are published or not. The documents may come from teaching and research institutions in France or abroad, or from public or private research centers.

L'archive ouverte pluridisciplinaire **HAL**, est destinée au dépôt et à la diffusion de documents scientifiques de niveau recherche, publiés ou non, émanant des établissements d'enseignement et de recherche français ou étrangers, des laboratoires publics ou privés.



Distributed under a Creative Commons Attribution - NonCommercial - NoDerivatives 4.0
International License

1 [Quesnel, Y. et al. \(2020\). Geophysical Signature of the Tunnunik Impact Structure, Northwest](#)
2 [Territories, Canada. *Meteoritics and Planetary Science*, 1-16, doi:10.1111/maps.13447](#)

3
4 **Geophysical Signature of the Tunnunik Impact Structure,**
5 **Northwest Territories, Canada**
6

7 **Y. Quesnel¹, W. Zylberman^{1,2}, P. Rochette¹, M. Uehara¹, J. Gattacceca¹, G. R. Osinski^{2,3},**
8 **Dussouillez, P.¹, Lepaulard, C.¹ and C. Champollion⁴**

9 ¹Aix-Marseille Univ, CNRS, IRD, INRAe, Coll France, CEREGE, Aix-en-Provence, France.

10 ²Institute for Earth and Space Exploration, University of Western Ontario, London, Ontario N6A
11 5B7, Canada

12 ³Department of Earth Sciences, University of Western Ontario, London, Ontario N6A 5B7,
13 Canada

14 ⁴Geosciences Montpellier, UMR5243, Université de Montpellier – CNRS, Place E. Bataillon,
15 34095 Montpellier, France

16
17 Corresponding author: Yoann Quesnel (quesnel@cerege.fr)
18

19 **Key Points:**

- 20 • A 3 mGal negative gravity anomaly and a 120 nT positive magnetic anomaly were
21 measured over the center of the Tunnunik impact structure
- 22 • A numerical model constrained by laboratory measurements on rock samples suggests an
23 uplifted magnetic crystalline basement
- 24 • The fracturing/brecciation extends down to 1 km in depth

26 **Abstract**

27 In 2011, the discovery of shatter cones confirmed the 28 km-diameter Tunnunik complex impact
28 structure, Northwest Territories, Canada. This study presents the first results of ground-based
29 electromagnetic, gravimetric and magnetic surveys over this impact structure. Its central area is
30 characterized by a ~10 km wide negative gravity anomaly of about 3 mGal amplitude, roughly
31 corresponding to the area of shatter cones, and associated with a positive magnetic field anomaly
32 of ~120 nT amplitude and 3 km wavelength. The latter correlates well with the location of the
33 deepest uplifted strata, an impact-tilted Proterozoic dolomite layer of the Shaler Supergroup
34 exposed near the center of the structure and intruded by dolerite dykes. Locally, electromagnetic
35 field data unveil a conductive superficial formation which corresponds to an 80-100 m thick sand
36 layer covering the impact structure. Based on measurements of magnetic properties of rock
37 samples, we model the source of the magnetic anomaly as the magnetic sediments of the Shaler
38 Supergroup combined with a core of uplifted crystalline basement with enhanced magnetization.
39 More classically, the low gravity signature is attributed to a reduction in density measured on the
40 brecciated target rocks and to the isolated sand formations. However, the present-day fractured
41 zone does not extend deeper than ~1 km in our model, indicating a possible 1.5 km of erosion
42 since the time of impact, about 430 Ma ago.

43

44 **Plain Language Summary**

45 *This study reveals the geophysical signature of the buried structure of an eroded impact crater,*
46 *Tunnunik, located in Northwest Territories, Canada. A positive magnetic anomaly was detected*
47 *at the center, showing the uplift of some deep geological formations and the possible presence of*
48 *strongly-magnetized basement. A negative gravimetric anomaly is also observed, mostly*
49 *corresponding to the fracturing/brecciation of the impacted rocks inside the crater. Using*
50 *numerical models constrained by laboratory measurements on rock samples, the physical*
51 *properties and geometry of the buried geological formations are estimated. An important*
52 *implication of this study is the link between the geophysical remains of an impact crater and the*
53 *post-impact erosion.*

54

55

INTRODUCTION

56 With about 190 impact structures confirmed, the Earth presents currently the lowest number of
57 craters of all the terrestrial planets. Indeed, craters on Earth are continuously removed by erosion
58 and hidden by sedimentation, and/or tectonic activity (Grieve 2006; Hergarten and Kenkmann
59 2015). Therefore, geophysical methods are particularly relevant to the study of terrestrial impact
60 craters, as they can reveal buried or eroded structures (Pilkington and Grieve 1992; Gudlaugsson
61 1993; Grieve and Pilkington 1996; Pilkington and Hildebrand 2000; Kjaer et al. 2018). They also
62 help to unveil the physical effects of syn- and post-impact processes which are still not
63 completely understood, particularly for mid-size to large impact structures (Osinski and Pierazzo
64 2013). Moreover, they help to reveal the present-day geometry of the different layers of impact
65 lithologies.

66 The most commonly used geophysical techniques for studying impact craters are gravity and
67 magnetic surveys by satellites, airplanes and/or ground measurements. Indeed potential-field
68 anomalies are often significant over impact structures, even buried or eroded. Small-size
69 (apparent diameter $D_a < 10$ km; D_a being the present-day diameter after erosion of the final crater
70 rim) impact craters are well characterized by negative potential field anomalies (Grieve and
71 Pilkington 1996), while it is not as clear for intermediate-size ($10 < D_a < 30$ km) complex impact
72 structures. The low gravity signature is due to a reduction in the density of target rocks because
73 of impact-induced fracturing, brecciation and melting due to the compression, excavation and
74 modification stages of the impact event (Pilkington and Grieve 1992; Osinski and Pierazzo
75 2013). Additional minor effects can also contribute to the mass deficiency, such as lower-density
76 post-impact sedimentary layers filling relatively fresh craters (Grieve and Pilkington 1996). The
77 lithological and physical changes associated with the impact process can also be modified by
78 post-impact alteration. The observed weak magnetic signature over small craters ($D_a < 10$ km)
79 results from the alteration of the pre-existing regional signals (Cisowski and Fuller 1978; Clark
80 1983; O'Neill and Heine 2005), but may be also influenced by the reduction of the natural
81 remanent magnetization (NRM) through partial or complete shock remagnetization (Gattacceca
82 et al. 2010). Overall, some of the impact induced effects on rock magnetism are still debated,
83 such as the possible preservation of a shock-induced remanent magnetization (SRM; e.g.,
84 Cisowski and Fuller 1978; Halls 1979; Pesonen et al. 1992; Gattacceca et al. 2007, 2008, 2010;
85 Tikoo et al. 2015). For larger craters ($D_a > 10$ km), central high-amplitude and short-wavelength
86 anomalies are observed (Pilkington and Grieve 1992; Morgan and Rebolledo-Vieyra 2013).
87 Their source is usually complex, and can originate from shock metamorphism (e.g., Slate Islands
88 and Charlevoix, see Halls 1979; Robertson and Roy 1979; review in Grieve and Pilkington
89 1996), cooling of impact-melt rocks and/or breccias (e.g., Ries and Morokweng; Pohl et al. 2010;
90 Henkel et al. 2002), structural deformation of target geological units during the modification
91 stage (e.g. Bosumtwi; Ugalde et al. 2007), and/or post-impact hydrothermal processes (e.g.,
92 Haughton: Quesnel et al. 2013; Zylberman et al. 2017; Clearwater Lakes: Gattacceca et al.
93 2019). Henkel (1992) and Henkel and Reimold (2002) also suggested oxidation of pre-existing
94 magnetic carrier phase in the strongly fractured rocks, which may explain the reduction of
95 ground magnetic susceptibilities surrounding the central uplift. The origin of magnetic anomalies
96 with a significant negative part in complex and eroded impact structures remains unclear
97 (Pilkington and Grieve 1992; Grieve 2006). All larger craters ($D_a > 40$ km) show high-amplitude
98 magnetic anomalies at their center (Pilkington and Grieve 1992; Morgan and Rebolledo-Vieyra
99 2013).

100 It is notable that the magnetic and gravimetric anomaly characterization strongly depends on the
101 altitude of the measurements: no signature at satellite or airborne altitude does not mean that
102 there are no contrasts in the upper crust of the studied area. For instance, this effect has been
103 suggested to explain the lack of 'apparent' magnetic signatures of Hellas and Argyre large
104 impact basins on Mars (Acuña et al. 1998), even if the absence of a dynamo during the cooling
105 stage after these events is a better explanation (Langlais et al. 2004; Langlais and Thébault
106 2011). This may also be suggested for most of the magnetic signatures of lunar impact structures:
107 the lowest satellite magnetic field measurements were performed at minimum 30 km of altitude,
108 excluding *de facto* the mapping of small-wavelength magnetized contrasts (Nicholas et al. 2007;
109 Hemingway and Tikoo 2018), while a wealth of gravimetric details were observed by the
110 GRAIL mission (Zuber et al. 2016). On Earth, few large impact structures – including Chicxulub
111 (Gulick et al. 2013) - exhibit a gravimetric anomaly that can be observed by satellite

112 measurements. For mid-size impact structures, the characterization of gravimetric and magnetic
113 anomalies by airplane/helicopter measurements can be possible to get a broad overview of its
114 geophysical signature. However, such airborne surveys are still low-resolution, practically
115 difficult and expensive for studying remote areas. Ground surveys allow acquiring high-
116 resolution gravimetric and magnetic data over impact structures in remote areas. also enable
117 sampling to be conducted for further laboratory analyses, to update the geological mapping and
118 to identify possible local geophysical anomalies (e.g., the Haughton crater center; Zylberman et
119 al. 2017). All these data will serve as constraints for modeling the geological (and possibly
120 multiple) sources of the observed gravimetric and magnetic anomalies. The central uplift itself
121 creates a gravimetric anomaly, but on Earth, the erosion level of the impact structure will then
122 play a role. In most cases, the more eroded the crater, the less significant (in wavelength and
123 amplitude) the gravimetric negative anomaly (Pilkington and Grieve 1992). On the other hand,
124 the erosion of a large thickness of post-impact sediments will better unveil density and
125 magnetization contrasts linked to pre-, syn- or post-impact processes in the structure.

126 In this study the first ground geophysical measurements acquired over the recently-discovered
127 mid-size ($D_a \sim 28$ km) eroded Tunnunik impact structure are described, analysed and modeled in
128 terms of geological structure and cratering processes.

129

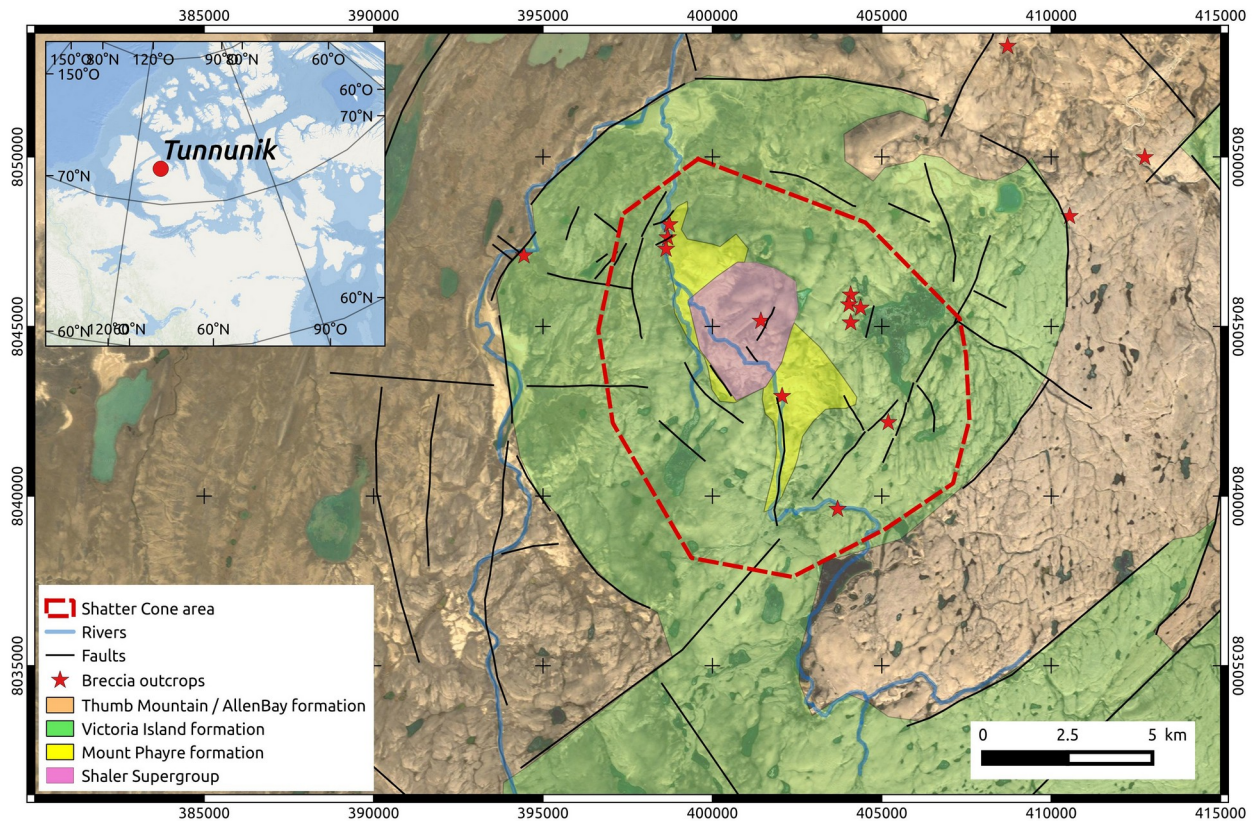
130

GEOLOGICAL CONTEXT

131 The Tunnunik impact structure is located in the western Canadian Arctic Archipelago (Fig. 1)
132 just south of the Richard Collinson Inlet (“Tunnunik” in Inuvialuit), on the Prince Albert
133 peninsula, northwestern Victoria Island ($72^{\circ}28'N$, $113^{\circ}58'W$). The target sequence is composed
134 of sub-horizontal Cambro-Silurian sedimentary rocks (mostly carbonates) from the Arctic
135 Platform: from oldest to youngest, the Wynniatt (part of the Shaler Supergroup), Mount Phayre,
136 Victoria Island, and Allen Bay formations (Fig. 1; Dewing et al. 2013; Newman and Osinski
137 2016). Neoproterozoic diabase dykes also intrude into the Wynniatt Fm. More detailed
138 information on the pre-impact stratigraphic sequence and geological context can be found in
139 Dewing et al. (2013). There are also a number of Quaternary sand and gravel formations (not
140 shown in Fig. 1) deposited between 50 and 100 m in altitude throughout the crater interior, and
141 mainly related to the central river valley where some outcrops of the Shaler Supergroup and
142 Mount Phayre formations show a central uplift. By using remote sensing and sample analyses,
143 this formation was recently mapped as fluvio-glacial deposits (Unit 1 of Choe et al. 2019). Sea
144 shells were found in some outcrops of this formation, suggesting that it could correspond to post-
145 glacial marine deltaic deposits, now overwater due to the isostatic rebound. Based on the
146 observation of tilted strata and the distribution of shatter cones, Dewing et al. (2013) described a
147 ~ 25 km-wide circular feature. Based on detailed mapping and the presence of inward-dipping
148 listric faults out to a radius of 14 km, Osinski et al. (2013) defined a 28 ± 0.5 km apparent crater
149 diameter (D_a). No crater fill breccias and/or melt rocks were mapped, indicating that the impact
150 structure is deeply eroded. Only isolated dykes of polymict impact breccias were observed
151 (Newman and Osinski 2016). Paleomagnetic analyses of these dykes has provided an age for the
152 impact event of 440 ± 10 Ma (Lepaulard et al. 2019). The present topography decreases from
153 about 200 m altitude in the southeast corner to the sea level of the Richard Collinson Inlet in the
154 northwest. This general trend is cut by two major $\sim N-S$ oriented rivers - including one in the

155 central part of the structure – and by syn-impact (mainly concentric) and post-impact (mainly in
 156 the SW-NE direction) faults. Therefore, except for the concentric faults, there is no topographical
 157 and geomorphological signature of an impact crater. Possible hydrothermal alteration has also
 158 been reported within the impact structure, but evidence remains sparse and samples are still
 159 under investigation, as it is not always clear if the described alteration is pre- or post-impact
 160 (Marion et al. 2013).

161



162 Fig. 1. Geological map of the Tunnunik impact structure, modified from Dewing et al. (2013) and
 163 Newman and Osinski (2016). Background corresponds to a Map Data ©2015 Google satellite image.
 164 Stratigraphy: Shaler Supergroup (Neoproterozoic), Mount Phayre formation (Cambrian), Victoria Island
 165 formation (Cambrian/Ordovician), and Thumb Mountain/Allen Bay formation (Upper
 166 Ordovician/Silurian). The coordinate system for the geological map is UTM Zone 12 North projection
 167 with WGS84 datum, in meters. Upper left: Location of the structure on Victoria Island in the Canadian
 168 Arctic, with a geographic coordinate system on a WGS84 datum. Background corresponds to the ArcGIS
 169 online ESRI Ocean layer.

170

171

METHODS

172 Ground gravity and magnetic field measurements (total paths of 300 km) were performed within
 173 the central part of the Tunnunik impact structure, in an area approximately corresponding to the
 174 extent of the Victoria Island Formation (Fig. 2). The wide N-S river on the western side
 175 prevented further measurements in that direction, while the large area and a short time in the

176 field in this remote Arctic region also influenced our choice to mainly survey the center of the
177 structure. Thus we obtained a well constrained map of the central part rather than extended
178 profiles. We also conducted local subsurface electromagnetic sounding in order to determine the
179 thickness of quaternary surficial formations that could influence the gravity signature.

180

181

182

183

184

185

186

187

188

189

190

191

192

193

194

195

196

197

198

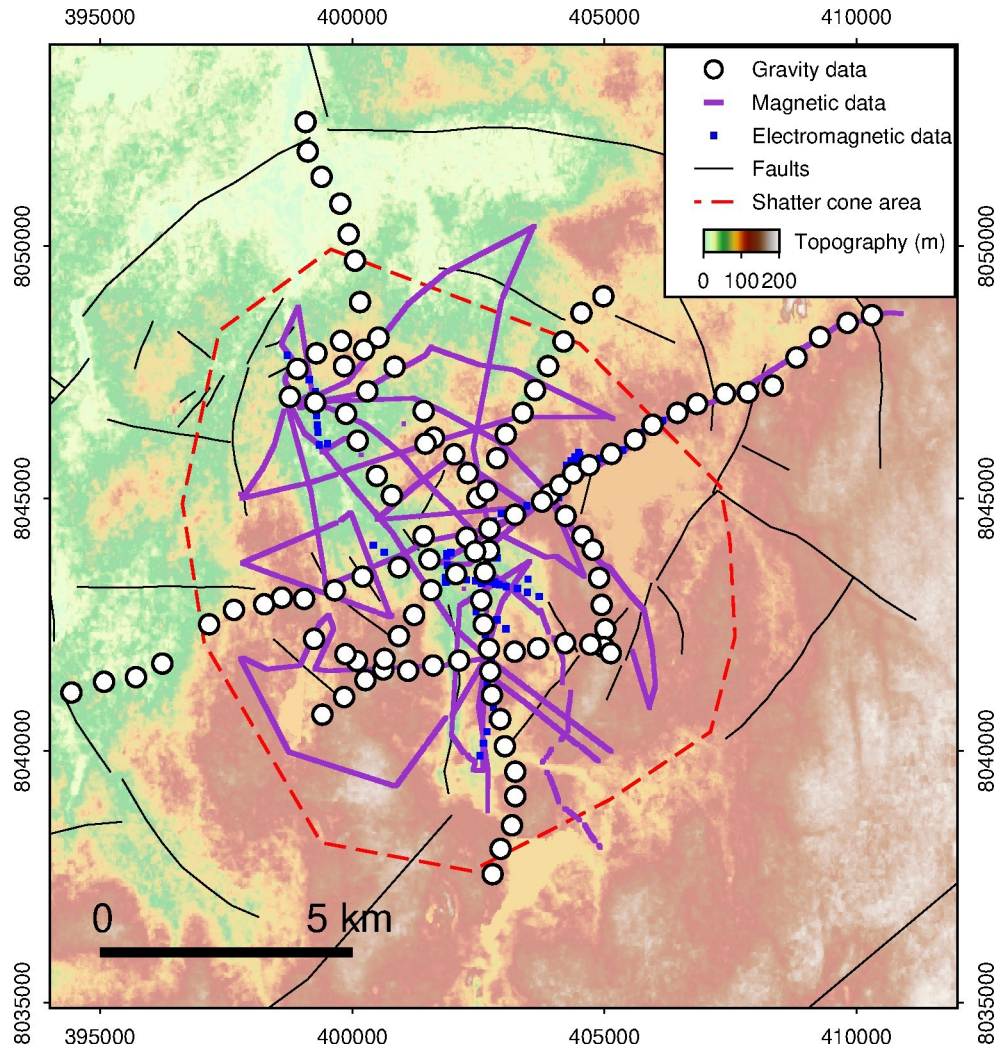
199

200

201

202

203



198 Fig. 2. Geophysical measurements performed at Tunnunik. Background corresponds to a digital elevation
199 model version 2 (GDEM2) from ASTER (NASA-METI). Same coordinate system as for Fig. 1.

201 The gravity field was measured using a Scintrex CG-5 Autograv gravity meter. Three main
202 profiles in the NNW-SSE, NE-SW and WSW-ENE directions were performed with a mean
203 spacing of 500 m between each measurement point. These profiles cross each other near the

204 estimated center of the structure. Additional measurements along 5 shorter profiles, with
205 acquisition spacing between 250 and 500 m, completed the central part of the gravity map. A
206 total of 113 independent measurements were acquired. For each point, the gravity field was
207 measured 4 times during 100 seconds at 1 Hz, excluding outliers and outputting the mean value.
208 Instrumental error (i.e. 1 sigma uncertainty), as defined by the standard deviation of the 4
209 successive averages, varied between 0.5 and 16 μGal with a mean value of 6 μGal , depending on
210 wind and soil stability. Depending on the number of acquired measurements, on the local
211 topography of the surveyed area, as well as on the weather conditions, drift varied from 0.5 to
212 2.6 $\mu\text{Gal mn}^{-1}$ (average: 1.2 $\mu\text{Gal mn}^{-1}$). For each station, the X, Y and Z locations were precisely
213 measured using a differential GNSS Trimble R8 system. The base and mobile GNSS stations
214 were connected by a standard radio communication and monitored with a controller. Due to the
215 long distances and topography, a secondary radio relay station was used to extend the
216 communication with the base station. With the real-time kinematics (RTK) capability of the
217 system, a precision of ± 10 cm in elevation (Z) was achieved. This precision is suitable for
218 gravity accuracy at the 0.1 mGal level as an elevation error of 10 cm produces a 0.03 mGal error
219 in free-air gravity (Featherstone and Dentith 1997). Then the Bouguer correction (0.1 mGal/m,
220 opposite sense to free-air) will reduce this error to 20 μGal , which, combined with the average 6
221 μGal experimental error of the CG-5 instrument, would result in a total error inferior to 30 μGal .
222 This total error is below 1% of the total amplitude of our Bouguer gravity anomaly (see next
223 sections). Gravity data were processed using the dGNSS elevation data and a series of standard
224 corrections to remove the Earth tide, drift, latitude, altitude and topographic effects and finally,
225 to obtain the complete Bouguer gravity anomaly value. The final accuracy of the Bouguer
226 anomaly (taking into account instrumental errors, altitude and topography correction accuracies)
227 is 0.1 mGal (see the Supplementary Material for details about gravity data processing, and Figs.
228 S1 and S2; GEOINT 2008; Heiskanen and Moritz 1967; Hwang et al. 2003; Schwiderski 1980;
229 Tamura 1987; Wenzel 1996).

230 The variations of the intensity of the geomagnetic field vector (Total Magnetic Intensity, TMI)
231 were mapped using a mobile Geometrics G-858 MagMapper cesium vapor probe fixed at 2 m
232 height on a pole. The internal and external field temporal variations on site were measured using
233 a fixed Geometrics G-856 proton precession base station magnetometer. The use of a base
234 station for diurnal variation of the magnetic field was necessary due to the proximity of the North
235 magnetic pole (1,700 km away): diurnal variations reached several hundreds of nT of amplitude
236 during our surveys, potentially completely concealing the crustal signal, which is in the range of
237 0 to 100 nT in amplitude. The G-856 and G-858 magnetometers have absolute precision of 0.1
238 and 0.01 nT (at 1 Hz sampling rate), respectively. A mean sampling rate of 15 s was used on the
239 field leading to a mean spatial resolution of ~ 20 m along each survey line. The surveyed area
240 was mainly restricted to the central part within the shatter cone area, except for one ENE-WSW
241 line which extends towards the northeast faults (Fig. 2). During the survey the IGRF predicted
242 average field was about 58140 nT in intensity - exactly in the range of our base station data - 86°
243 and 16° of inclination and declination, respectively. Given the magnetic north pole was 1,700 km
244 away, there was no need to apply the reduction-to-the-pole to our magnetic field data. The
245 magnetic field anomaly was then simply computed by subtracting the TMI value measured at the
246 base station from the TMI value acquired by the mobile magnetometer. We carefully checked
247 that there was no correlation of the anomaly spatial variations with the topography. The poor
248 spatial resolution of the available airborne data (CAN-SCAN project 1965-1976) and magnetic
249 field grids in this area (Ravat et al. 2009) prevents from a good characterization and comparison

250 of the regional influence over the impact structure. Therefore, we first applied a low-pass (100
251 m) filter to the interpolated data grid to exclude isolated outliers, and then detrended this grid by
252 a 3rd-order polynomial surface to level the anomaly map (i.e. to remove an eventual large-scale
253 regional crustal field signal).

254 Local electromagnetic soundings were performed using the Geonics Ltd EM34-3 terrain
255 conductivity meter, which measures the apparent conductivity (sensitivity of 1000 mS.m⁻¹) of the
256 ground by means of a pair of coils. We measured 104 data points to characterize the lateral and
257 vertical extent of quaternary sand deposits at different locations nearby the main central river
258 (Fig. 2). Both horizontal and vertical dipole configurations were implemented at distances of 10,
259 20, and 40 m between the transmitter and receiver coils, to increase the investigated depth (see
260 Supplementary Material; McNeill 1980). The mean distance between each measurement point
261 was 250 m.

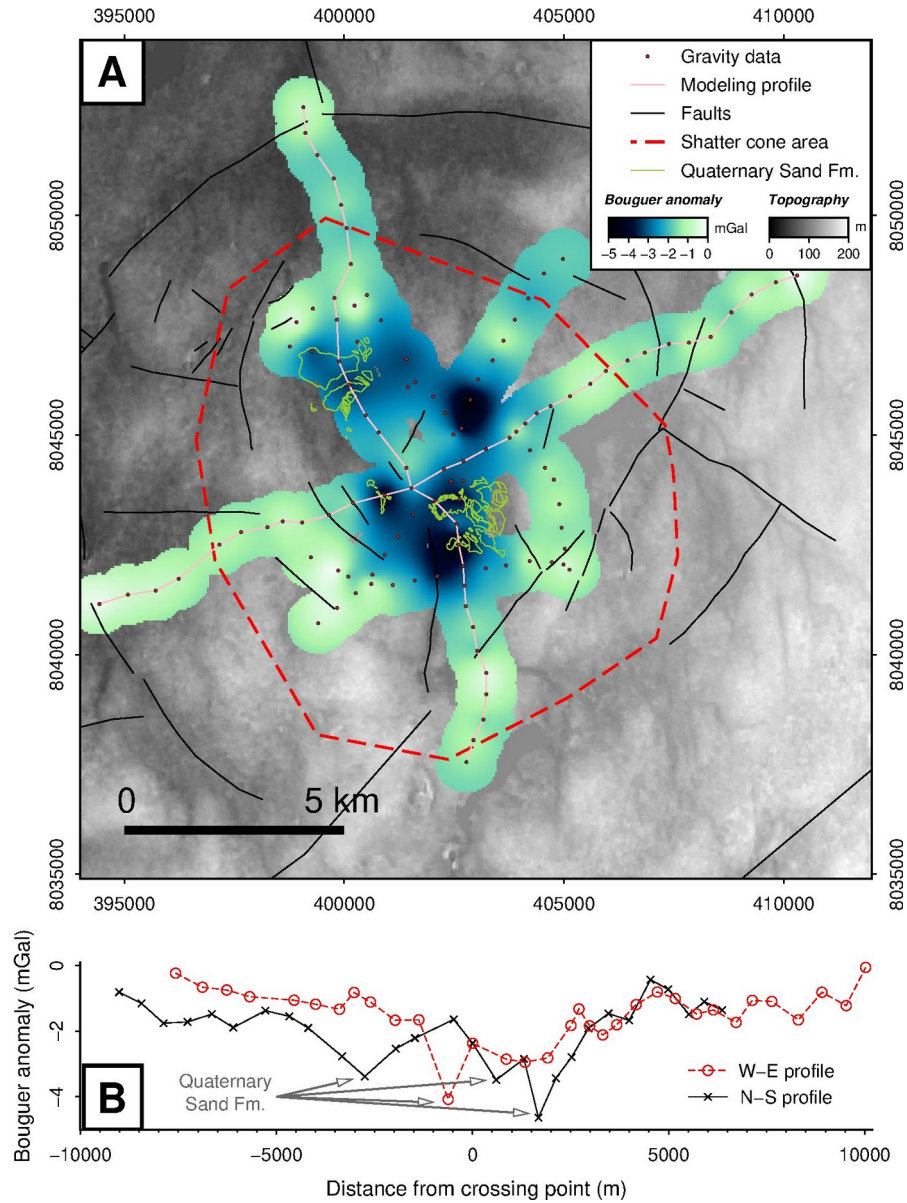
262 In addition to these geophysical data, we also sampled all accessible lithologies to measure some
263 petrophysical properties in laboratory in order to constrain numerical models of the geological
264 sources of the observed geophysical anomalies. The bulk density of these samples was measured
265 using a Quantachrome Helium stereopycnometer. Magnetic parameters used to constrain the
266 model are described in Lepaulard et al. (2019): the remanent magnetization intensity was
267 obtained from measurements with a Superconducting Quantum Interference Devices (SQUID)
268 760R (2G Entreprises) magnetometer while the magnetic susceptibility was measured with an
269 AGICO Kappabridge MFK1.

270

271

RESULTS AND INTERPRETATION

272 The complete Bouguer gravity anomaly map is shown in Fig. 3A. It was generated using a
273 minimum curvature interpolation and masking areas with no data. Despite the influence of radial
274 line surveys, the map reveals a general negative gravity anomaly of ~3 mGal amplitude and ~10
275 km of wavelength over the center of the Tunnunik impact structure. In the absence of data
276 outside of the surveyed area, we cannot infer that this is the maximum amplitude of the anomaly
277 observed over this impact structure (i.e. 3 mGal is a lower limit for the amplitude of the
278 anomaly). In detail, the shape of this central anomaly does not appear to be circular but seems
279 slightly more extended in the N-S direction. The minimum value of -4.6 mGal is also not at the
280 center but is located in a ring of about -4 to -4.5 mGal anomalies surrounding a less negative (-
281 2.5 mGal) isolated central anomaly; this is considered to be located near the center of the
282 structure (402000, 8044000). Fig. 3A shows that most of the concentric negative extrema
283 correspond to the Quaternary sand deposits, suggesting that this porous formation may locally
284 amplify the general low gravity signal at the center. Fig. 3B shows that 5 km away from the
285 center, the anomaly gradients are less important, but still a small increase is observed at the
286 borders, arguing in favor of a more extended anomaly. Therefore, we conclude that a central
287 negative anomaly is visible, with a possible asymmetric shape and with a possible extension
288 beyond our survey area. This gravity anomaly is not observed in the regional gravity data
289 acquired by the National Research Council of Canada (see Supp. Mat. for details of calculations
290 and regional trends in Fig. S1).



292

293

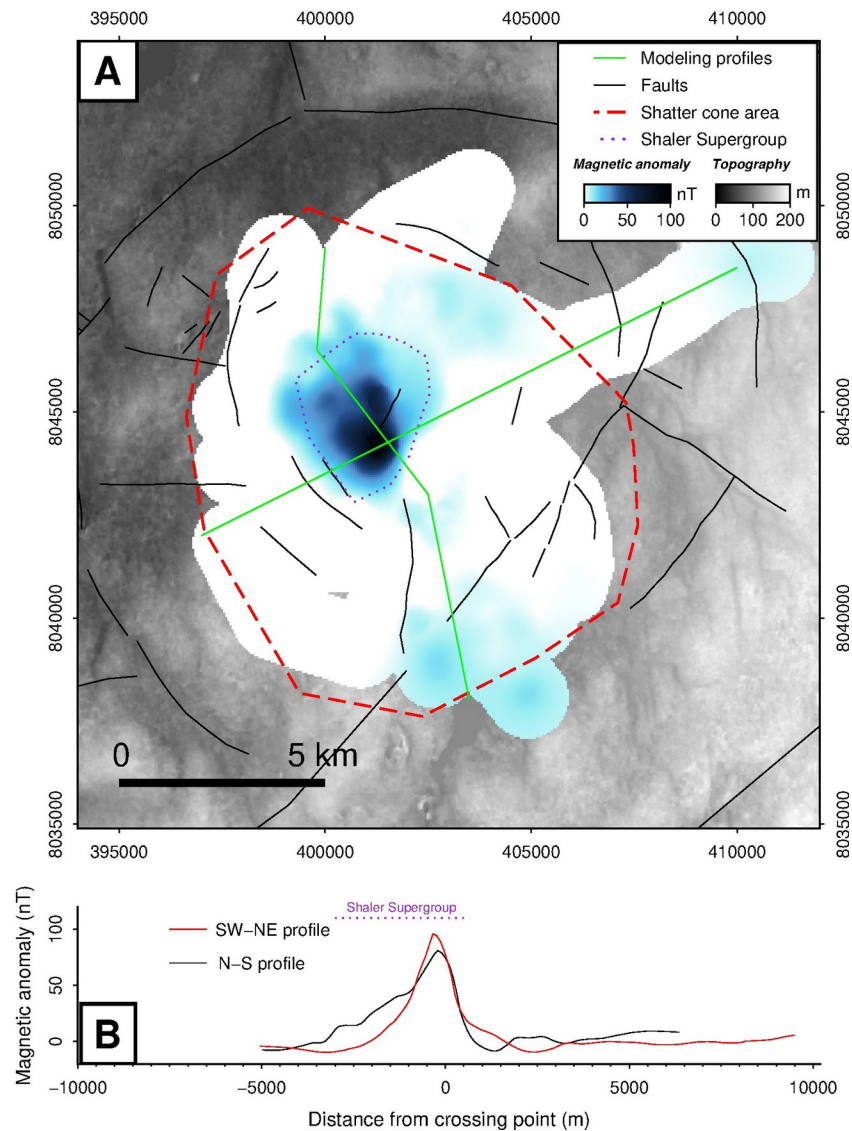
294

295 Fig. 3. (A) Complete Bouguer gravity anomaly map over the center of the Tunnunik impact structure. The
 296 thin pink lines correspond to the gravity anomaly profiles selected for modeling and shown in (B). Faults
 297 are indicated by full black lines. The area where shatter cones were observed and collected is delimited by
 298 the dashed red line (Osinski and Ferrière 2016), while the limits of the Quaternary Sand Formation
 299 correspond to the thin green lines. Grayscaled background corresponds to the digital elevation model
 300 shown in Fig. 2. Same coordinate system as for Fig. 1. (B) Complete Bouguer gravity anomaly data along
 301 the selected profiles in (A).

302 The interpolated map of the total-field magnetic anomaly over the center of the Tunnunik impact
 303 structure is shown in Fig. 4A. The data distribution limits the analysis to the central part (i.e.
 304 within the shatter cone area) only. The total amplitude of the interpolated and filtered signal
 305 reaches 120 nT, with minimum and maximum values of -20 and 96 nT, respectively. The
 306 positive part of the anomaly is restricted to the central area of the structure and centered at
 307 401000, 8045000. It correlates well with the Shaler Supergroup (with intruding diabase dykes)
 308 outcrops (Fig. 4A). Compared to the gravity anomaly, the center of the positive anomaly is
 309 located ~500 m away in the NW direction, but on average, the observed central negative
 310 gravimetric and positive magnetic anomalies overlap. Although less extended than the Bouguer
 311 gravity anomaly, the central positive magnetic field anomaly also seems to be slightly
 312 asymmetrical with a major axis in the NNW–SSE direction and a minor axis in the WSW–ENE
 313 direction, with wavelengths of ~6 and ~4 km respectively. Fig. 4B shows the shape of the
 314 anomaly in the N-S and W-E directions, unveiling this weak asymmetry.

315

316

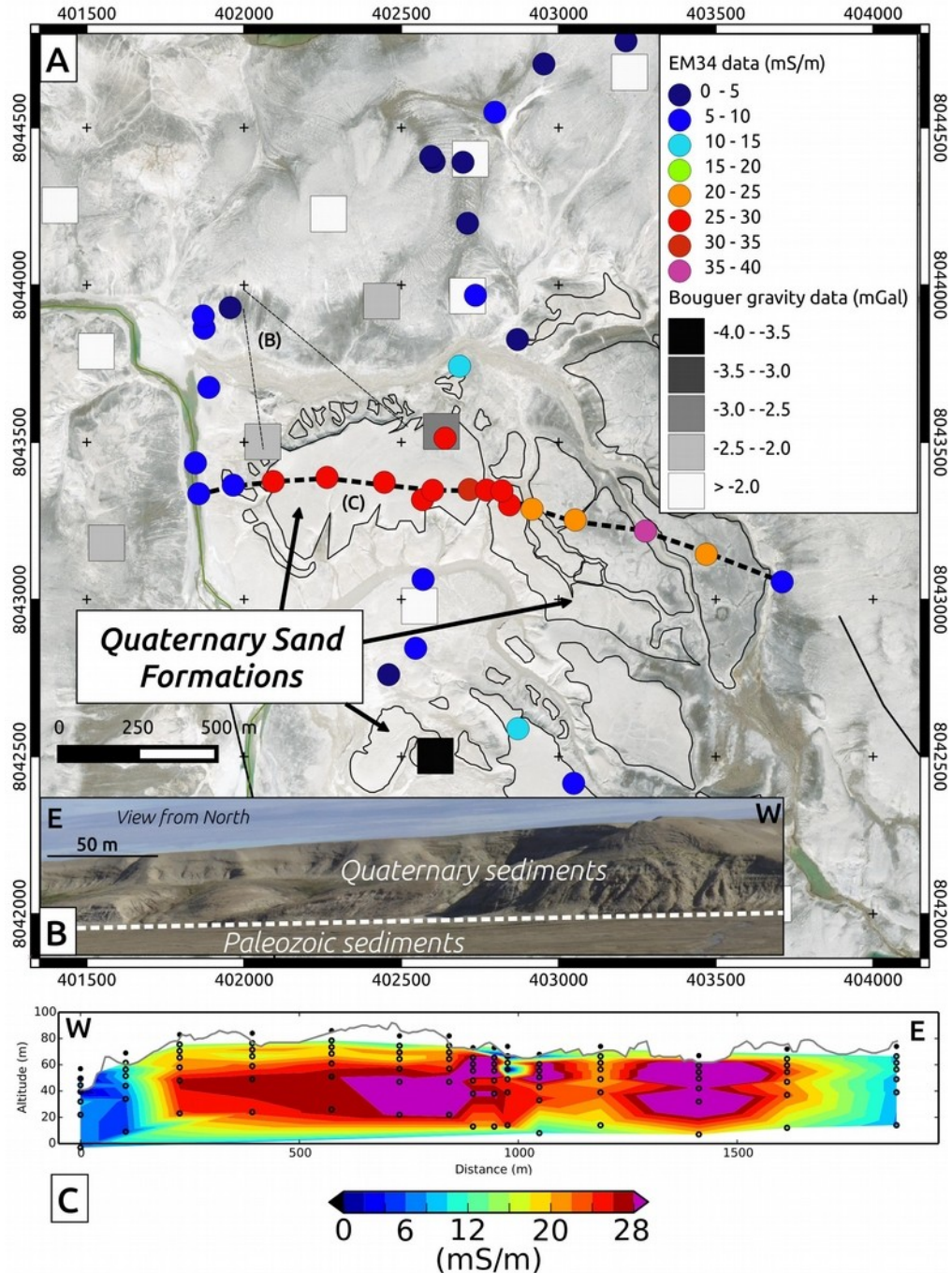


317 Fig. 4. (A) Magnetic field anomaly map of the center of the Tunnunik impact structure. The green solid
318 line corresponds to the locations of the data selected for modeling. Faults are indicated by full black lines.
319 The area where shatter cones were observed and collected is delimited by the dashed red line (Osinski and
320 Ferrière 2016). The area where the Shaler Supergroup Formation is exposed is delimited by the dotted
321 purple line. Grayscaled background corresponds to the digital elevation model shown in Fig. 2. Same
322 coordinate system as for Fig. 1. (B) Magnetic field anomaly along the selected profiles in (A).

323 Thus, both gravity and magnetic field signals show a significant anomaly of several km
324 wavelength in the surveyed area. Their correlation argues in favor of a possible single geological
325 source at or nearby the center of the impact structure.

326 Fig. 5A shows the spatial variations of the subsurface electrical conductivity derived from the
327 electromagnetic measurements performed in the central area of the impact structure (see Supp.
328 Mat. for results of EM surveys performed outside this central part). It clearly reveals that the hills
329 around the center and nearby the river contain porous liquid water loaded material (> 20 mS/m)
330 that contrasts with the resistive frozen soil outside these areas (< 5 mS/m; see Todd et al. 1991
331 for a comparison in the same environment). The conductive material corresponds to the sand
332 formations either originated from fluvio-glacial processes (Choe et al. 2019) or deposited by sea
333 level variations during Quaternary era (Fig. 5B). Within these deposits, variations of the
334 conductivity between 10 and 30 mS/m are observed, reflecting possible variations in the amount
335 of pore water and its salinity eventually due to presence of fossil sea water. Presence of
336 permafrost below the liquid water layer is also a possibility, while permafrost formation above it
337 may have been prevented by a thick dry sand layer (Fig. 5C). The conductivity remains high at
338 the maximum possible depths reached by our measurements, indicating that this sand formation
339 is thicker than 60-80 m. This observation is important because such a thick, weakly dense ($2,000$
340 kg m^{-3}), material will decrease the Bouguer gravity value for data acquired on top of (or nearby)
341 this formation. In fact, most of the lowest gravity anomalies correspond to the location of these
342 deposits (see Fig. 5A for an example of the correlation with gravity low values). Still, on
343 kilometric scale, there is a general, centered and negative ~ 3 mGal Bouguer gravity anomaly
344 over the center of the impact structure.

345



347 Fig. 5. (A) Map of the electrical conductivity variations at about 20 m in depth, in the central area of the
 348 impact structure. Bouguer gravity data are also shown to illustrate the correlation between some isolated
 349 low gravity values and the Quaternary Sand deposits. Dashed black line corresponds to the cross-section
 350 shown in (C). (B) Image of the conductive formation composed of Quaternary sediments nearby the
 351 central river. (C) W-E cross-section resulting from interpolation of conductivity data (vertical
 352 exaggeration ~ 2 ; points: data from different coil orientations at each location) acquired on the sand
 353 formation in the same area, along the dashed line in (A).

354

355

356

357

358

DISCUSSION

Diameter and erosion

359 Tunnunik is a mid-size impact structure with a ~ 10 km wavelength negative Bouguer gravity
360 anomaly of ~ 3 mGal amplitude over its center. Mid-size complex impact craters (see Osinski and
361 Grieve 2013 for a review) are typically characterized by circular negative gravity anomalies that
362 extend to or beyond the crater diameter. The size and amplitude of the anomaly are expected to
363 increase with an increasing apparent crater diameter D_a (Pilkington and Grieve 1992; Grieve and
364 Pilkington 1996). Since our measurements are limited to the center of the impact structure, they
365 do not reach the outermost faults (outside the map in Fig. 2), which represent the outer limit of
366 D_a , as defined in Osinski et al. (2013). Thus, we can expect a larger amplitude and wavelength of
367 the low gravity signal observed at Tunnunik: the Bouguer gravity data towards the rims still
368 show – in all directions – a small increase before reaching the regional signal (here leveled to 0
369 mGal). The minimum amplitude of the anomaly (~ 3 mGal) could reflect a deeply-eroded
370 structure, because impact structures of comparable size generally have a higher amplitude (e.g.,
371 10 mGal for Keurusselkä; Raiskila et al. 2013). Alternatively, this amplitude could be due to the
372 type of target rocks: impact structures in sedimentary targets generally have lower maximum
373 negative Bouguer gravity anomalies (Δg) than those in crystalline targets (Pilkington and Grieve
374 1992).

375 Impact structures can be classified using the erosional level index (E) established by Dence
376 (1972; see also Grieve and Robertson 1979) and based on the preservation of their ejecta, crater-
377 fill products and exposure of crater floor (Pilkington and Grieve 1992). Most of the indicated
378 diameters in impact studies are apparent crater diameters D_a (Osinski and Pierazzo 2013).
379 Indeed, the majority of complex impact craters on Earth are eroded (i.e., they are impact
380 structures) and therefore only D_a can be determined in most cases. Tunnunik seems to correspond
381 to the worst state of preservation: indeed the crater floor has been removed and the substructure
382 exposed, with no remnant of ejecta or crater-fill deposits preserved (Dewing et al. 2013; Osinski
383 et al. 2013; Newman and Osinski 2016). The only preserved impact breccia found in the field are
384 in the form of very local and thin (< 1 m of width) dykes injected into the sedimentary target
385 rocks (Osinski et al. 2013; Newman and Osinski 2016). Slightly modifying the index definition,
386 Osinski and Ferrière (2016) classified the Tunnunik structure as erosion state 6, because of these
387 still visible isolated breccia dikes. Such a deep level of erosion can be either due to a particularly
388 old impact structure or to an especially high rate of erosion, or both. In the present-day
389 periglacial environment of the Canadian High Arctic archipelago (e.g., Lee and Osinski 2005),
390 the 23 Ma Haughton impact structure, located about 900 km away, has been relatively well
391 preserved. Haughton is characterized by a $D_a \approx 23$ km and a smaller estimated rim-to-rim
392 diameter (D) of 16 km (Osinski et al. 2005). Its negative Bouguer gravity anomaly has a 12
393 mGal amplitude and a 24 km wavelength, the latter being very similar to its D_a (Pohl et al.,
394 1988). It has an erosional level of 2, which means that it is relatively fresh with ejecta partly
395 preserved (Osinski and Ferrière 2016). As mentioned earlier, the diameter of the gravity anomaly
396 should be roughly equal to D_a in relatively fresh craters such as Haughton, while the amplitude -
397 more affected by erosion - is not a relevant criterion (Pilkington and Grieve 1992). Therefore,

398 our gravimetric data suggest that the Tunnunik impact structure is severely eroded, in agreement
399 with its old age. Indeed, using paleomagnetism, Lepaulard et al. (2019) estimated that this impact
400 event occurred 430-450 Ma ago.

401 A similarly eroded impact structure is Gosses Bluff in Australia (Barlow 1979), which also
402 formed in sedimentary target rocks. Its apparent crater diameter D_a has been recently revised to
403 32 km (Osinski and Ferrière 2016). Its total gravimetric anomaly is $\Delta g = -5.5$ mGal with a central
404 peak (CP) of -3.5 mGal ($\Delta g = -3$ to -4 mGal and CP = -2.5 mGal at Tunnunik). This 142.5 Ma
405 impact structure has been attributed an erosion level similar to Tunnunik ($E = 6-7$; Pilkington
406 and Grieve 1992; Osinski and Ferrière 2016), while the presence of crater-fill breccias should
407 revise this value to $E = 5$ (Milton and Sutter 1987). Nevertheless, it shows that the relatively
408 weak amplitude of the remaining gravity anomaly at Tunnunik is not a unique case.

409 Besides, another phenomenon could explain this feature, without requiring a high amount of
410 erosion. Indeed, diagenetic pressure-solution (Sprunt 1977) could cement the impact-induced
411 fracturation in target rocks buried below a few kilometers of post-impact sediments. To our
412 knowledge, this post-impact phenomenon was never invoked before as a possible way to reduce
413 the amplitude of gravity anomalies in impact structures in sedimentary carbonated rocks. Long
414 term healing of impact induced carbonate porosity by pressure-solution is a well-known
415 phenomena (Croizet et al. 2013) that may be particularly effective in the Tunnunik limestones
416 due to the several hundreds Myr of burial endured by the fractured rock. Moreover, as the impact
417 occurred around 430-450 Ma ago, soon after deposition of the Ordovician sediments, this target
418 may have been not fully lithified, resulting in a lesser amount of fracturing and/or easier healing
419 of fractures. Possibly, it could be a new factor contributing to the generally weaker maximum
420 negative Bouguer gravity values for impact structures associated with sedimentary targets
421 (Pilkington and Grieve 1992). Lastly, the effect of central uplift of underlying basement has to be
422 taken into account, as it can partly cancel the broad negative anomaly in the structure center, as
423 described for example in the 6 km diameter Jebel Waqf as Suwwan structure (Heinrichs et al.
424 2014).

425

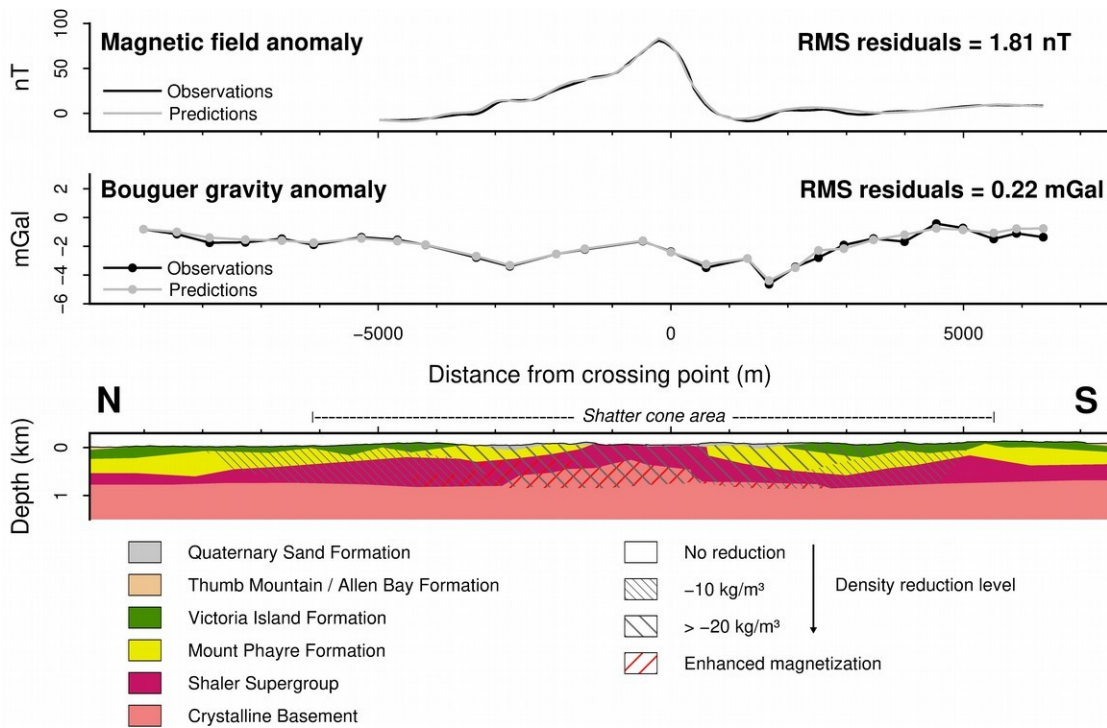
426 **Modeling the Tunnunik impact structure and post-impact erosion**

427 A possible geological solution explaining the observed gravity and magnetic field anomalies
428 over the center of the Tunnunik impact structure is shown in Fig. 6. This numerical model is
429 constrained by (1) gravity and magnetic field data, (2) average values of the bulk density for the
430 Earth's layers such as the crust and the mantle (not shown in Fig. 6), (3) measured physical
431 parameters for the different geological formations identified and sampled in the field, *i.e.*, bulk
432 densities, magnetic susceptibility, natural remanent magnetization (NRM) intensity, inclination
433 (I) and declination (D), and (4) field geological data and mapping, *i.e.*, thickness of geological
434 formations (Dewing et al. 2013) and location of structures such as contacts and faults (Newman
435 and Osinski 2016). Table 1 shows the measured physical parameters used in the model.
436 Consistent with geological mapping, the model shows the remains of a central uplift with the
437 Shaler Supergroup in the very centre. Clear lateral physical contrasts may reflect faults,
438 particularly if they join some mapped faults on surface. Near the center (*i.e.*, ± 2 km from the
439 profile center), the uplift of sedimentary units likely occurred along thrust faults (some are
440 mapped and shown on Fig. 1). The crystalline basement core of this central uplift underlying the

441 Shaler formation seems affected by brecciation and/or fracturing, as well as by an enhancement
442 of its magnetization intensity, required to explain the central magnetic anomaly detected on Fig.
443 4. The shape of the strongly-magnetized crystalline basement body contributes to the skewness
444 of the anomaly (see profiles on Fig. 4B). Nearby this basement core, the deep part of the Shaler
445 Supergroup unit also possesses a magnetization intensity larger than the overlying and
446 surrounding parts, but about 10 times weaker than the one of the crystalline basement. More
447 dolerite dykes may be present at depth in this unit. Overall, ~5 km from the center, coinciding
448 with the shatter cone area, and from 0.7 to 1 km in depth at the center, the rocks seem more
449 brecciated and fractured than outside, with 20 to 100 kg/m³ density reduction (*i.e.* a maximum of
450 4% of porosity increase). This is probably the most striking result of this study: even if the
451 Tunnunik impact structure is highly eroded and even if the Quaternary Sand Formation biases
452 the general low gravity signal by producing isolated very low (down to -4.6 mGal) gravity
453 values, a ~1 km-thick zone of brecciated and fractured uplifted rocks (including basement) seems
454 to be present. The presence of crystalline basement rocks (denser than the overlying units despite
455 brecciation) in the central uplift also accounts for the local gravity ‘high’ of -2.6 mGal at the
456 center of the structure, within the general gravity low. There is also a transition zone of density
457 reduction (~10 kg/m³) between 5 and 10 km of lateral distance from the center, inside the rim of
458 local faults that surrounds our studied area (see Figs. 1 and 2).

459 A second model was built along the W-E direction profiles and is shown in the Supplementary
460 Material (Fig. S3). It reveals a structure similar to the one shown in the N-S model of Fig. 6,
461 again with ~1 km-thick brecciated/fractured rocks at the center, and with an associated
462 enhancement of magnetization. The combination of these 2 perpendicular profiles does support a
463 small asymmetry of the brecciated rocks towards N (Fig. 6), but not really towards W (Fig. S3).
464 Of course, in the absence of data with higher spatial resolution (especially gravity data) and of
465 borehole data, more detailed geological models (including 3D representation) are not possible.
466 The pre-impact distribution of densities within the target rocks is also a key parameter in those
467 models (Pilkington and Grieve 1992). Despite stratigraphic information from Dewing et al.
468 (2013), our models show that sharp and significant (e.g. ~300 m for some layers in the central
469 area) thickness variations are necessary to explain the observed anomalies. This variability is due
470 to faulting which offsets formations, including the Mount Phayre Formation which has a weak
471 density (~2,500 kg/m³). The porous Quaternary sand units, possibly thicker than 100 m (as
472 shown by EM34 measurement interpretation) and correlated with the very low gravity values,
473 also play a role in decreasing the RMS residuals (of about 0.2 mGal) between observations and
474 predictions of the Bouguer gravity signal.

475



477 Fig. 6. N-S profile modeling of the Tunnunik impact structure constrained by magnetic and gravity data,
 478 as well as by laboratory measurements on samples. Top: comparison of observed (black) and predicted
 479 (gray) magnetic and gravity anomaly data. Location of the gravity measurements are shown by the solid
 480 points. Bottom: corresponding forward numerical model of the crust over the center of the Tunnunik
 481 impact structure. The physical parameters of each layer are shown in Table 1. Fracturing and brecciation
 482 (symbolized by gray hatching) decrease the bulk density values of all geological layers from the outer
 483 parts of the crater to the center. Topographic variations are from the global digital elevation model
 484 version 2 (GDEM2) of ASTER (NASA-METI). No vertical exaggeration.

485 Table 1. Physical parameters of the Tunnunik geological layers

Geological unit	$D^{1,2}$ (kg m ⁻³)	K^1 (10 ⁻³ SI)	NRM ¹ (A.m ⁻¹)	I^1 (°)	D^1 (°)
Quaternary sand formation	2000	-	-	-	-
Thumb Mountain / Allen Bay formation	2740-2760	0.02	$< 10^{-3}$	-	-
Victoria Island formation	2720-2750	0.01	$< 10^{-3}$	-	-
Mount Phayre formation	2470-2580	0.07	$< 10^{-3}$	-	-
Shaler Supergroup (with dolerite dykes) ³	2630-2650	0.04 – 0.2	0.01 – 0.03	80-90	0
Crystalline basement ⁴	2650-2700	50	0.1 – 0.5	90	0

486 ¹d, bulk density; K, volumic magnetic susceptibility; NRM, natural remanent magnetization; I and D, inclination and declination
 487 of NRM, respectively

488 ²Minimum bulk density values are associated with rock samples collected nearby the center (i.e. distance < 5 km from modeling
 489 profile center), while maximum values correspond either to samples collected far from the center (i.e. $d \sim 8-10$ km) or to values
 490 expected from the forward modeling (e.g., for the upper crust basement).

491 ³The Shaler Supergroup rocks are intruded by dolerite dykes of $K = 4 \cdot 10^{-2}$ SI, $NRM = 0.7$ A.m⁻¹, $I \sim 30^\circ$, $D \sim 110^\circ$ (Lepaulard et al.,
 492 2019). Therefore we adjusted the parameters of the corresponding modeled layer by considering about 5% of dolerite dykes.

493 ⁴The basement with an enhanced magnetization is correlated to the basement affected by brecciation (see Fig. 6).

494

495 Despite the simplicity of the models, there is a good agreement with computed estimations of
 496 brecciation/fracture depth extent in the presence of a low gravity anomaly. Indeed, according to
 497 the infinite slab model formula (see Supp. Mat. for calculation) for structures of $D_a \geq 20\text{-}30$ km
 498 (Pilkington and Grieve 1992), a maximum density contrast of 100 kg m^{-3} (Table 1), associated
 499 with a maximum negative gravity value $\Delta g = -3$ to -4 mGal, gives a maximum depth extent $Z =$
 500 715 to 954 m, a value in the range of the depth extent ($0.7\text{-}1$ km) of the brecciated/fractured zone
 501 of our models (Figs. 6 and S3). A density contrast of about 150 kg m^{-3} has been determined at
 502 Gosses Bluff (Barlow 1979), a structure similar to Tunnunik (see discussion above). However,
 503 the determination of density contrasts between unfractured and fractured target rocks remains
 504 sparse (see Pilkington and Grieve 1992 for a list). Similarly, for deeply eroded structures ($E = 6\text{-}$
 505 7 ; Grieve and Robertson 1979), the amount of removal of the disturbed zone beneath the crater
 506 floor is poorly constrained, allowing for significant variations in the corresponding gravity effect
 507 (Pilkington and Grieve 1992).

508 At Haughton, the expected post-impact erosion (~ 150 m; Osinski et al. 2005) together with the
 509 age of the structure (~ 23.5 Ma; Young et al. 2013) lead to an average erosion rate of 6.4 m Ma^{-1}
 510 since the time of the impact. Because Tunnunik is at high latitudes in an expected relatively
 511 stable tectonic environment of the Canadian Arctic since about $150\text{-}200$ Ma, we can suppose as
 512 first approximation the same erosion rate as Haughton to obtain a minimum estimate of the
 513 erosion at Tunnunik. Using the paleomagnetic age of ~ 430 Ma for the Tunnunik impact structure
 514 (Lepaulard et al. 2019) with Haughton's erosion rate of 6.4 m Ma^{-1} , it gives ~ 2.7 km of post-
 515 impact erosion. Using only 200 Ma with the same rate, it leads to ~ 1.3 km. One could argue that
 516 this post-impact erosion is responsible for the weakness of the observed negative Bouguer
 517 gravity anomaly. However, because the impact indeed happened ~ 430 Ma in the Silurian or in
 518 the late Ordovician, the target was "only" composed of the Allen Bay (Ordovician-Silurian),
 519 Victoria Island (Ordovician), Stripy Unit (Cambrian) and Wynnai (Proterozoic) formations
 520 which are observed in the structure (Dewing et al. 2013). Therefore, only the younger impacted
 521 unit (Allen Bay) could have been partially eroded away. Its thickness is supposed to be of
 522 maximum ~ 1 km (Dewing et al. 2013). Combined with the possible uncertainty in paleomagnetic
 523 dating, this could give a maximum thickness of about 1 km for the target rocks possibly eroded
 524 away. One cannot assess the thickness of post-impact deposits, but between 430 and ~ 200 Ma,
 525 the Tunnunik impact structure moved from equatorial to high latitudes. It implies possible higher
 526 erosion rates during this period, which may compensate the deposition of sediments. The
 527 apparent crater diameter D_a shrinks with increasing depth of erosion Z_E by $D_a = D - 1.15 Z_E$,
 528 because of the inclination of crater rim normal faults which dip toward the center of the crater by
 529 generally 60° (Kenkmann et al. 2013). According to this relation, and supposing $Z_{E\text{min}} = 1$ km
 530 (erosion of target rocks), $Z_{E\text{max}} = 2.7$ km (total erosion) and a $D_a = 28$ km, the final (rim-to-rim)
 531 diameter D of the fresh Tunnunik impact crater could have been between ~ 29 km and ~ 31 km.

532

533

Magnetization contrasts

534 The positive magnetic field anomaly detected over the center of the Tunnunik impact structure
535 appears to almost exactly correlate to the outcrop area of the Wynniatt (part of the Shaler
536 Supergroup) Formation (Figs. 1 and 4). Similar to Haughton, the most magnetic rock mapped
537 and collected in the area is dolerite ($K = 4 \cdot 10^{-2}$ SI and $\text{NRM} = 0.7 \text{ A}\cdot\text{m}^{-1}$ in average). This mafic
538 rock is present as localized dykes intrusive into the crystalline basement and into the Shaler
539 Supergroup units (Dewing et al. 2013). To take into account these mafic dykes in our forward
540 model, we considered that 5% of the volume of this formation was composed of dolerite,
541 resulting in a maximum magnetization intensity of $0.03 \text{ A}\cdot\text{m}^{-1}$ with a magnetic susceptibility of 2
542 $\cdot 10^{-1}$ SI (Table 1). These values are several orders of magnitude higher than the NRM and K of all
543 other sedimentary rocks present in the area (therefore considered with $M = 0 \text{ A}\cdot\text{m}^{-1}$ in the
544 modeling). However, our models show that an additional deeper strongly-magnetized ($0.5 \text{ A}\cdot\text{m}^{-1}$)
545 source is needed to explain the shape and amplitude of the central magnetic anomaly (Figs. 6 and
546 S3). As mentioned in the previous sections, we suggest that this could be uplifted crystalline
547 basement rocks. Such magnetized crystalline blocks within the central uplift could be explained
548 either by the intrusion of dykes of impact melt rocks and breccias with a significant thermal
549 remanent magnetization (e.g., Shah et al. 2005), or by shock-induced magnetization of pre-
550 impact rocks (Cisowski and Fuller 1978), or by an enhanced magnetization of the basement due
551 to hydrothermal alteration (Quesnel et al. 2013). The latter has been shown to increase the NRM
552 within impact melt rocks of the central uplift at the nearby Haughton impact structure
553 (Zylberman et al. 2017). Another possibility would be a concentration of mafic, pre-impact
554 magmatic rocks at local scale, possibly remagnetized by the impact. Of course, a combination of
555 these different processes is still possible.

556

557 **Conclusion**

558 The first geophysical measurements within the Tunnunik impact structure indicate the existence
559 of a central ~ 10 km wavelength negative Bouguer gravity anomaly of ~ 3 mGal and a positive
560 magnetic anomaly of ~ 120 nT amplitude. It shows that, despite the highly-eroded state of the
561 structure, the geophysical signature of the impact structure is still preserved. Using forward
562 modeling constrained by petrophysics measurements, the geometry of the sources accounting for
563 these anomalies is estimated. It reveals a fractured zone down to 0.7-1 km depth in its present-
564 day state, and suggests that at least 1 km of erosion has occurred since 430-450 Ma, the time of
565 impact. The positive magnetic field anomaly is suggested to be mainly due to uplifted crystalline
566 basement, but also by the Shaler Supergroup sedimentary formation which is intruded by dolerite
567 dykes. The origin of the magnetization's enhancement for the crystalline basement is still
568 unknown, even if impact-generated hydrothermal activity is a good candidate.

569 To decipher the issues unveiled by these first measurements and by modeling, additional
570 gravimetric data would be helpful and other geophysical methods could be used across the whole
571 structure, like seismics and/or magnetotellurics which could reveal the deep
572 velocity/conductivity contrasts between fractured/brecciated and pristine crystalline basement at
573 depth.

574

575 **Acknowledgments, Samples, and Data**

576

577 IPEV is acknowledged for funding the field work (project “Tunnunik”, #1139). Excellent logistical support from the Polar
578 Continental Shelf Project is also gratefully acknowledged. This work has been carried out thanks to the support of the A*MIDEX
579 grant (n°ANR-11-IDEX-0001-02) funded by the French Government “Investissements d’Avenir” program. MITACS and Campus
580 France are thanked for facilitating international collaboration by providing the MITACS Globalink Research Award-Campus
581 France to W.Z. The Scintrex CG-5 relative gravimeter was loaned by the Gravity-Mobile facility (GMOB) of RESIF-INSU
582 (CNRS). This work was also supported by the Programme National de Planétologie (PNP) of INSU-CNRS, co-funded by CNES,
583 as well as by a CNRS Projet International de Coopération Scientifique (PICS n°263407 – GEOCRAT). Funding from the Natural
584 Sciences and Engineering Research Council of Canada to GRO is gratefully acknowledged.

585 **References**

586 Acuna M. H., Connerney J. E. P., Wasilewski P., Lin R. P., Anderson K. A., Carlson C. W.,
587 McFadden J., Curtis D. W., Mitchell D., Reme H., Mazelle C., Sauvaud J. A., d’Uston C., Cros
588 A., Medale J. L., Bauer S. J., Cloutier P., Mayhew M., Winterhalter D., and Ness N. F. 1998.
589 Magnetic field and plasma observations at Mars: initial results of the Mars Global Surveyor
590 Mission. *Science* 279: 1676-1680.

591
592 Barlow B. C. 1979. Gravity investigations of the Gosses Bluff impact structure, central Australia.
593 *Journal of Australian Geology and Geophysics* 4: 323-339.

594
595 CAN-SCAN project 1965-1976. *Canadian-Scandinavian Digital Data*. Dept Energy, Mines and
596 Resources of Canada. These data are stored at NOAA NCEI website
597 (<https://www.ngdc.noaa.gov/mgg/trk/aeromag/can-scan/can-scan.htm>)
598

599 Choe B.-H., Tornabene L., Osinski G. R., and Newman J. 2019. Remote Predictive Mapping of
600 the Tunnunik Impact Structure in the Canadian Arctic using Multispectral and Polarimetric SAR
601 Data Fusion. *Canadian Journal of Remote Sensing*. doi:10.1080/07038992.2018.1544846

602
603 Cisowski S. M., and Fuller M. 1978. The effect of shock on the magnetism of terrestrial rocks.
604 *Journal of Geophysical Research* 83: 3441-3458. doi:10.1029/JB083iB07p03441

605
606 Clark J. F. 1983. Magnetic survey data at meteoritic impact sites in North America. *Geomagnetic*
607 *Service of Canada, Earth Physics Branch, Open File* 83-5: 1-32.

608
609 Croizet D., Renard F., and Gratier J.-P. 2013. Chapter 3 - Compaction and porosity reduction in
610 carbonates: A review of observations, theory, and experiments. *Advances in Geophysics* 54: 181
611 238. doi:10.1016/B978-0-12-380940-7.00003-2

612
613 Dence M. R. 1972. *The nature and significance of terrestrial impact structures*. 24th Int. Geol.
614 Congr., 77-89.

615
616 Dewing K., Pratt B. R., Hadlari T. Brent T., Bédard J., and Rainbird R. H. 2013. Newly
617 identified
618 “Tunnunik” impact structure, Prince Albert Peninsula, northwestern Victoria Island, Arctic
619 Canada. *Meteoritics and Planetary Science* 48(2): 211-223. doi:10.1111/maps.12052

620
621 Featherstone W.E., and Dentith, M.C. 1997. A geodetic approach to gravity reduction for
622 geophysics. *Computer Geosciences* 23: 1063-1070.

623

- 624 Gattacceca J., Lamali A., Rochette P., Boustie M., and Berthe L. 2007. The effects of explosive
625 driven shocks on the natural remanent magnetization and the magnetic properties of rocks.
626 *Physics of the Earth and Planetary Interiors* 162: 85-98. doi:10.1016/j.pepi.2007.03.006
627
- 628 Gattacceca J., Berthe L., Boustie M., Vadeboin F., Rochette P., and De Resseguier T. 2008. On
629 the efficiency of shock magnetization processes. *Physics of the Earth and Planetary Interiors*
630 166: 1-10. doi:10.1016/j.pepi.2007.09.005
631
- 632 Gattacceca J., Boustie M., Lima E., Weiss B. P., de Resseguier T., and Cuq-Lelandais J. P. 2010.
633 Unraveling the simultaneous shock magnetization and demagnetization of rocks. *Physics of the*
634 *Earth and Planetary Interiors* 182: 42-49. doi:10.1016/j.pepi.2010.06.009
635
- 636 Gattacceca J., Zylberman W., Coulter A.B., Demory F., Quesnel Y., Rochette P., Osinski G.R.,
637 and Brenuchon E. 2019. Paleomagnetism and rock magnetism of East and West Clearwater Lake
638 impact structures. *Canadian Journal of Earth Sciences* 56(9); 983-993. doi:10.1139/cjes-2018-
639 0291
640
- 641 GEOINT 2008. *Gravity station data format and anomaly computations*. National Geospatial-
642 Intelligence Agency of the USA, 6.
643
- 644 Grieve R. A. F. 2006. *Impact structures in Canada*. 1st ed. St Johns: Geological Association of
645 Canada.
646
- 647 Grieve R. A. F., and Pilkington M. 1996. The signature of terrestrial impacts. *AGSO Journal of*
648 *Australian Geology and Geophysics* 16(4): 399-420.
649
- 650 Grieve R. A. F., and Robertson P. B. 1979. The Terrestrial Cratering Record. 1. Current Status of
651 Observations. *Icarus* 38: 212-229. doi:10.1016/0019-1035(79)90179-9
652
- 653 Gudlaugsson S. T. 1993. Large impact crater in the Barents Sea. *Geology* 21(4): 291-294.
654 doi:10.1130/0091-7613(1993)021<0291:LICITB>2.3.CO;2
655
- 656 Gulick S. P. S., Christeson G. L., Barton P. J., Grieve R. A. F., Morgan J. V., and Urrutia-
657 Fucugauchi J. 2013. Geophysical characterization of the Chicxulub impact crater. *Reviews of*
658 *Geophysics* 51: 31-52. doi:10.1002/rog.20007
659
- 660 Halls H. C. 1979. The Slate Islands meteorite impact site: A study of shock remanent
661 magnetization. *Geophysical Journal International* 59(3): 553-591. doi:10.1111/j.1365-
662 246X.1979.tb02573.x
663
- 664 Heinrichs T., Salameh E., and Khouri H. 2014. The Waqf as Suwwan crater, Eastern Desert of
665 Jordan: aspects of the deep structure of an oblique impact from reflection seismic and gravity
666 data. *International Journal of Earth Science* 103: 233-252. doi:10.1007/s00531-013-0930-4
667
- 668 Heiskanen W. A., and Moritz H. 1967. *Physical Geodesy*. Edited by J. Gilluly and A. O.
669 Woodford. San Francisco: W. H. Freeman and Company.

- 670
671 Hemingway D. J., and Tikoo S. M. 2018. Lunar Swirl Morphology Constrains the Geometry,
672 Magnetization, and Origins of Lunar Magnetic Anomalies. *Journal of Geophysical Research -*
673 *Planets* 123. doi:10.1029/2018JE005604
- 674
675 Henkel H. 1992. Geophysical aspects of meteorite impact craters in eroded shield environment,
676 with special emphasis on electric resistivity. *Tectonophysics* 216: 63-89. doi:10.1016/0040-
677 1951(92)90156-Z
- 678
679 Henkel H., and Reimold, W.U. 2002. Magnetic model of the central uplift of the Vredefort
680 impact structure, South Africa. *Journal of Applied Geophysics* 51: 43-62.
- 681
682 Henkel H., Reimold W. U., and Koeberl C. 2002. Magnetic and gravity model of the
683 Morokweng impact structure. *Journal of Applied Geophysics* 49: 129-147. doi:10.1016/S0926-
684 9851(01)00104-5
- 685
686 Hergarten S., and Kenkmann, T. 2015. The number of impact craters on Earth: Any room for
687 further discoveries?. *Earth and Planetary Science Letters* 425: 187-192.
688 doi:10.1016/j.epsl.2015.06.009
- 689
690 Hwang C., Wang C.-G., and Hsiao Y.-S. 2003. Terrain correction computation using Gaussian
691 quadrature. *Computers and Geosciences* 29: 1259-1268.
- 692
693 Kenkmann T., Collins G. S., and Wünnemann K. 2013. The modification stage of crater
694 formation. In *Impact cratering: processes and products*, edited by Osinski G.R. and Pierazzo E.
695 Malaysia: Wiley-Blackwell. pp. 60-75
- 696
697 Kjær K. H. Larsen N. K., Binder T., Bjørk A. A., Eisen O., Fahnestock M. A., Funder S., Garde
698 A. A., Haack H., Helm V., Houmark-Nielsen M., Kjeldsen K. K., Khan S. A., Machguth H.,
699 McDonald I., Morlighem M., Mouginot J., Paden J. D., Waight T. E., Weikusat C., Willerslev
700 E., and MacGregor J. A. 2018. A large impact crater beneath Hiawatha Glacier in northwest
701 Greenland. *Science Advances* 4: eaar8173. doi:10.1126/sciadv.aar8173
- 702
703 Langlais, B., Purucker, M. E., and Mandea, M., 2004. Crustal magnetic field of Mars. *Journal of*
704 *Geophysical Research* 109. doi:10.1029/2003JE002048 (E02008).
- 705
706 Langlais B., and Thébaud E. 2011. Predicted and observed magnetic signatures of martian
707 (de)magnetized impact craters. *Icarus* 212: 568-578. doi:10.1016/j.icarus.2011.01.015
- 708
709 Lee P., and Osinski G. R. 2005. The Haughton-Mars Project: Overview of science investigations
710 at the Haughton impact structure and surrounding terrains, and relevance to planetary studies.
711 *Meteoritics and Planetary Science* 40: 1755-1758. doi:10.1111/j.1945-5100.2005.tb00144.x
- 712
713 Lepaulard, C., Gattacceca, J., Swanson-Hysell, N., Quesnel, Y., Demory, F. and Osinski, G.
714 2019. A Paleozoic age for the Tunnunik impact structure. *Meteoritics and Planetary Science*
715 54(4): 740-751. doi:10.1111/maps.13239
- 716

- 717 Marion C. L., Osinski G. R., and Linnen R. L. 2013. *Characterization of hydrothermal*
718 *mineralization at the Prince Albert impact structure, Victoria Island, Canada (abstract #1635).*
719 44th Lunar and Planetary Science Conference, The Woodlands, Texas.
720
- 721 McNeill J. D. 1980. *Electromagnetic terrain conductivity measurement at low induction numbers*
722 (Technical Note TN-6). Mississauga, Ontario, Canada: Geonics Ltd.
723
724
725
- 726 Milton D. J., and Sutter J. F. 1987. Revised age for the Gosses Bluff impact structure, Northern
727 Territory, Australia, based on $^{40}\text{Ar}/^{39}\text{Ar}$ dating. *Meteoritics* 22: 281-289.
728
- 729 Morgan J., and Rebolledo-Vieyra M. 2013. Geophysical studies of impact craters. In *Impact*
730 *cratering: processes and products*, edited by Osinski G.R. and Pierazzo E. Malaysia: Wiley-
731 Blackwell. pp. 211-222
732
- 733 Newman J. D., and Osinski G. R. 2016. *Geological mapping of the Tunnunik impact structure,*
734 *Victoria Island, Canadian High Arctic (abstract #1591).* 47th Lunar and Planetary Science
735 Conference, The Woodlands, Texas.
736
- 737 Nicholas J. B., Purucker M. E., and Sabaka T. J. 2007. Age spot or youthful marking: Origin of
738 Reiner Gamma. *Geophysical Research Letters* 34: L02205. doi:10.1029/2006GL027794
739
- 740 O'Neill C., and Heine C. 2005. Reconstructing the Wolfe Creek meteorite impact: Deep
741 structure of the crater and effects on target rock. *Australian Journal of Earth Sciences* 52:699-
742 709. doi:10.1080/08120090500170450
743
- 744 Osinski G. R., and Ferrière L. 2016. Shatter cones: (Mis)understood? *Science Advances* 2(8): 9 p.
745 doi:10.1126/sciadv.1600616
746
- 747 Osinski G. R., and Grieve R. A. F. 2013. Comparison of mid-size terrestrial complex impact
748 structures: a case study. In *Impact cratering: processes and products*, edited by Osinski G.R. and
749 Pierazzo E. Malaysia: Wiley-Blackwell. pp. 290-305
750
- 751 Osinski G. R., and Pierazzo E. 2013. Impact cratering: processes and products. In *Impact*
752 *cratering: processes and products*, edited by Osinski G.R. and Pierazzo E. Malaysia: Wiley-
753 Blackwell. pp. 1-20
754
- 755 Osinski G. R., Lee P., Spray J. G., Parnell J., Lim D. S. S., Bunch T. E., Cockell C. S., and Glass
756 B. 2005. Geological overview and cratering model for the Haughton impact structure, Devon
757 Island, Canadian High Arctic. *Meteoritics and Planetary Science* 40: 1759-1776.
758 doi:10.1111/j.1945-5100.2005.tb00145.x
759
- 760 Osinski G. R., Abou-Aly S., Francis R., Hansen J., Marion C. L., and Tornabene L. L. 2013. *The*
761 *Prince-Albert structure, Northwest Territories, Canada: A new 28-km diameter complex impact*

- 762 structure (abstract #2099). 44th Lunar and Planetary Science Conference, The Woodlands,
763 Texas.
- 764
- 765 Pesonen L. J., Marcos N., and Pipping F. 1992. Palaeomagnetism of the Lappajärvi impact
766 structure, western Finland. *Tectonophysics* 216: 123-142. doi:10.1016/0040-1951(92)90160-8
767
- 768 Pilkington M., and Grieve R. A. F. 1992. The Geophysical Signature of Terrestrial Impact
769 Craters. *Reviews of Geophysics* 30(2): 161-181. doi:10.1029/92RG00192
770
- 771 Pilkington M., and Hildebrand A. R. 2000. Three-dimensional magnetic imaging of the
772 Chicxulub Crater. *Journal of Geophysical Research* 105(B10): 23,479-23,491.
773 doi:10.1029/2000JB900222
774
- 775 Pohl J., Eckstaller A. and Robertson P. B. 1988. Gravity and magnetic investigations in the
776 Haughton impact structure, Devon Island, Canada. *Meteoritics* 23: 235-238.
777
- 778 Pohl J., Poschlod K., Reimold W. U., Meyer C., and Jacob J. 2010. Ries crater, Germany: The
779 Enkingen magnetic anomaly and associated drill core SUBO 18. *Special Paper of the Geological*
780 *Society of America* 465: 141-163.
781
- 782 Quesnel Y., Gattacceca J., Osinski G. R., and Rochette P. 2013. Origin of the central magnetic
783 anomaly at the Haughton impact structure, Canada. *Earth and Planetary Science Letters* 367:
784 116-122. doi:10.1016/j.epsl.2013.02.032
785
- 786 Raiskila S., Plado J., Ruotsalainen H., and Pesonen L. J. 2013. Geophysical Signatures of the
787 Keurusselkä Meteorite Impact Structure - Implications for Crater Dimensions. *Geophysica* 49(1-
788 2): 3-23.
789
- 790 Ravat D., Finn C., Hill P., Kucks R., Phillips J., Blakely R., Bouligand C., Sabaka T., Elshayat
791 A., Aref A., and Elawadi E. 2009. A preliminary, full spectrum, magnetic anomaly grid of the
792 United States with improved long wavelengths for studying continental dynamics--A website for
793 distribution of data. *U.S. Geological Survey Open-File Report* 1258: 2 p.
794
- 795 Robertson P. B., and Roy J. L. 1979. Shock-diminished paleomagnetic remanence at the
796 Charlevoix impact structure, Quebec. *Canadian Journal of Earth Science* 16(9): 1842-1856.
797
- 798 Schwiderski E. W. 1980, Ocean tides, II: A hydrodynamic interpolation model. *Marine Geodesy*
799 3: 219-255.
800
- 801 Shah A., Brozena J., Vogt P., Daniels D., and Plescia J. 2005. New surveys of the Chesapeake
802 Bay impact structure suggest melt pockets and target-structure effect. *Geology* 33(5): 417-420.
803 doi:10.1130/G21213.1
804
- 805 Sprunt E. S. 1977. Destruction of porosity through pressure solution. *Geophysics* 42(4): 726-741.
806 doi:10.1190/1.1440742
807

- 808 Tamura Y. 1987. A harmonic development of the tide generating potential. *Bulletin*
809 *d'Informations des Marées Terrestres* 99: 6813–6855.
- 810 Tikoo S.M., J. Gattacceca, Swanson-Hysell, N. L., Weiss, B. P., Suavet, C., and Cournède, C.
811 2015. Preservation and detectability of shock-induced magnetization. *Journal of Geophysical*
812 *Research - Planets* 120. doi:10.1002/2015JE004840
- 813
- 814 Todd B.J., Pullan S.E., Hunter J.A. 1991. Electromagnetic studies across lakes and rivers in
815 permafrost terrain, Mackenzie River Delta, Northwest Territories, Canada. *Expanded Abstracts*
816 *of 61st Annual International Meeting, 10-14 Nov., Society of Exploration Geophysicists*, Tulsa,
817 Oklahoma, US, 565-568. doi:10.1190/1.1889198
- 818 Ugalde H., Morris W. A., Pesonen L. J., and Danuor S. K. 2007. The Lake Bosumtwi meteorite
819 impact structure, Ghana - Where is the magnetic source? *Meteoritics and Planetary Science*
820 42(4/5): 867-882.
- 821
- 822 Wenzel, H.-G. 1996. The Nanogal software: earth tide data processing package ETERNA 3.30.
823 *Bulletin d'Informations des Marées Terrestres* 124: 9425–9439.
- 824
- 825 Young K. E., Soest M. C., Hodges K. V., Watson E. B., Adams B. A., and Lee P. 2013. Impact
826 thermochronology and the age of Haughton impact structure, Canada. *Geophysical Research*
827 *Letters* 40: 3836-3840. doi:10.1002/grl.50745
- 828
- 829 Zuber M. T., Smith D. E., Neumann G. A., Goossens S., Andrews-Hanna J. C., Head J. W.,
830 Kiefer W. S., Asmar S. W., Konopliv A. S., Lemoine F. G., Matsuyama I., Melosh H. J.,
831 McGovern P. J., Nimmo F., Phillips R. J., Solomon S. C., Taylor G. J., Watkins M. M.,
832 Wicczorek M. A., Williams J. G., Jansen J. C., Johnson B. C., Keane J. T., Mazarico E.,
833 Miljković K., Park R. S., Soderblom J. M., and Yuan D.-N. 2016. Gravity Field of the Orientale
834 Basin from the Gravity Recovery and Interior Laboratory Mission. *Science* 354(6311): 438-441.
835 doi:10.1126/science.aag0519
- 836
- 837 Zylberman W., Quesnel Y., Rochette P., Osinski G. R., Marion C., and Gattacceca J. 2017.
838 Hydrothermally-enhanced magnetization at the center of the Haughton impact structure?
839 *Meteoritics and Planetary Science* 52(10): 2147-2165. doi:10.1111/maps.12917
- 840

841 **Figure captions**

842

843 Fig. 1. Geological map of the Tunnunik impact structure, modified from Dewing et al. (2013) and
844 Newman and Osinski (2016). Background corresponds to a Map Data ©2015 Google satellite image.
845 Stratigraphy: Neoproterozoic → Shaler Supergroup (Neoproterozoic), Cambrian → Mount Phayre
846 formation (Cambrian), Cambrian/Ordovician → Victoria Island formation (Cambrian/Ordovician), and
847 Thumb Mountain/Allen Bay formation (Upper Ordovician/Silurian). The coordinate system for the
848 geological map is UTM Zone 12 North projection with WGS84 datum, in meters. Upper left: Location of
849 the structure on Victoria Island in the Canadian Arctic, with a geographic coordinate system on a WGS84
850 datum. Background corresponds to the ArcGIS online ESRI Ocean layer.

851

852 Fig. 2. Geophysical measurements performed at Tunnunik. Background corresponds to a digital elevation
853 model version 2 (GDEM2) from ASTER (NASA-METI). Same coordinate system as for Fig. 1.

854

855 Fig. 3. (A) Complete Bouguer gravity anomaly map over the center of the Tunnunik impact structure. The
856 thin pinkwhite lines corresponds to the gravity anomaly profiles selected for modeling and shown in (B).
857 Faults are indicated by full black lines. The area where shatter cones were observed and collected is
858 delimited by the dashed red line (Osinski and Ferrière 2016), while the limits of the Quaternary Sand
859 Formation correspond to the thin green lines. Grayscaled background corresponds to the digital elevation
860 model shown in Fig. 2. Same coordinate system as for Fig. 1. (B) Complete Bouguer gravity anomaly
861 data along the selected profiles in (A).

862

863 Fig. 4. (A) Magnetic field anomaly map of the center of the Tunnunik impact structure. The green solid
864 line corresponds to the locations of the data selected for modeling. Faults are indicated by full black lines.
865 The area where of shatter cones were observed and collected is delimited by the dashed red line (Osinski
866 and Ferrière 2016). The area where outcrops the Shaler Supergroup Formation is exposed is delimited
867 by the dotted purple line. Grayscaled background corresponds to the digital elevation model shown in Fig. 2.
868 Same coordinate system as for Fig. 1. (B) Magnetic field anomaly along the selected profiles in (A).

869

870 Fig. 5. (A) Map of the electrical conductivity variations at about 20 m in depth, in the central area of the
871 impact structure. Bouguer gravity data are also shown to illustrate the correlation between some isolated
872 low gravity values and the Quaternary Sand deposits. Dashed black line corresponds to the cross-section
873 shown in (C). (B) Image of the conductive formation composed of Quaternary sediments nearby the
874 central river. (C) W-E cross-section resulting from interpolation of conductivity data (vertical
875 exaggeration ~ 2; points: data from different coil orientations at each location) acquired on the sand
876 formation in the same area, along the dashed line in (A).

877

878 Fig. 6. N-S profile modeling of the Tunnunik impact structure constrained by magnetic and gravity data,
879 as well as by laboratory measurements on samples. Top: comparison of observed (black) and predicted
880 (gray) magnetic and gravity anomaly data. Location of the gravity measurements are shown by the solid
881 points. Bottom: corresponding forward numerical model of the crust over the center of the Tunnunik
882 impact structure. The physical parameters of each layer are shown in Table 1. Fracturing and brecciation
883 (symbolized by gray hatching) decrease the bulk density values of all geological layers from the outer
884 parts of the crater to the center. Topographic variations are from the global digital elevation model
885 version 2 (GDEM2) of ASTER (NASA-METI). No vertical exaggeration.

886